

# <sup>8</sup>Evaluation of Precipitation Vertical Profiles Estimated by GPM-Era Satellite-Based Passive Microwave Retrievals

Nobuyuki Utsumi,  $^{a,b}$  F. Joseph Turk,  $^a$  Ziad S. Haddad,  $^a$  Pierre-Emmanuel Kirstetter,  $^{c,d,e,f}$  and Hyungjun Kim $^{a,g,h}$ 

a Jet Propulsion Laboratory, California Institute of Technology, Pasadena, California
b Nagamori Institute of Actuators, Kyoto University of Advanced Science, Kyoto, Japan
c School of Meteorology, University of Oklahoma, Norman, Oklahoma
d School of Civil Engineering and Environmental Science, University of Oklahoma, Norman, Oklahoma
c Advanced Radar Research Center, National Weather Center, Norman, Oklahoma
f NOAA/National Severe Storms Laboratory, Norman, Oklahoma
g Joint Institute for Regional Earth System Science and Engineering, University of California, Los Angeles, Los Angeles, California
h Institute of Industrial Science, The University of Tokyo, Tokyo, Japan

(Manuscript received 1 July 2020, in final form 5 October 2020)

ABSTRACT: Precipitation estimation based on passive microwave (MW) observations from low-Earth-orbiting satellites is one of the essential variables for understanding the global climate. However, almost all validation studies for such precipitation estimation have focused only on the surface precipitation rate. This study investigates the vertical precipitation profiles estimated by two passive MW-based retrieval algorithms, i.e., the emissivity principal components (EPC) algorithm and the Goddard profiling algorithm (GPROF). The passive MW-based condensed water content profiles estimated from the Global Precipitation Measurement Microwave Imager (GMI) are validated using the GMI + Dual-Frequency Precipitation Radar combined algorithm as the reference product. It is shown that the EPC generally underestimates the magnitude of the condensed water content profiles, described by the mean condensed water content, by about 20%–50% in the middle-to-high latitudes, while GPROF overestimates it by about 20%–50% in the middle-to-high latitudes and more than 50% in the tropics. Part of the EPC magnitude biases is associated with the representation of the precipitation type (i.e., convective and stratiform) in the retrieval algorithm. This suggests that a separate technique for precipitation type identification would aid in mitigating these biases. In contrast to the magnitude of the profile, the profile shapes are relatively well represented by these two passive MW-based retrievals. The joint analysis between the estimation performances of the vertical profiles and surface precipitation rate shows that the physically reasonable connections between the surface precipitation rate and the associated vertical profiles are achieved to some extent by the passive MW-based algorithms.

KEYWORDS: Precipitation; Microwave observations; Remote sensing; Satellite observations

#### 1. Introduction

Global precipitation products capitalize upon the long period of record of satellite-based passive microwave (MW) radiometer observations (Aonashi and Ferraro 2020). The passive MW brightness temperature (TB) represents the net top-of-atmosphere upwelling radiation, after taking into consideration the emission and scattering properties of hydrometeors within the top-to-bottom profile, including the contribution from the surface emissivity. The surface precipitation represents the net flux of the condensed water at the bottom of this profile as seen from space and is arguably

Oenotes content that is immediately available upon publication as open access.

Corresponding author: Nobuyuki Utsumi, utsumi.nobuyuki@kuas.ac.jp

one of the quantities that the TB is least directly sensitive to (Haddad et al. 2017). Furthermore, precipitation that falls near the surface is a manifestation of its associated vertical precipitation structure nearby and above. This implies that a more representative passive MW algorithm would have an ability to jointly estimate the vertical structure and the surface precipitation.

Some of the passive MW-based techniques estimate the precipitation vertical structure as well as the surface precipitation rate. For example, the Goddard profiling algorithm (GPROF) (Kummerow et al. 2015) for NASA's Global Precipitation Measurement (GPM) mission provides the hydrometeor vertical profiles as a standard output. There are also the passive MW-based techniques more specifically developed for estimating the vertical precipitation profiles (e.g., Evans et al. 1995; Skofronick-Jackson and Wang 2000; Bauer and Mugnai 2003; Haddad and Park 2009).

However, nearly all validation studies to date examine only the surface precipitation rate. A major difficulty with

DOI: 10.1175/JHM-D-20-0160.1

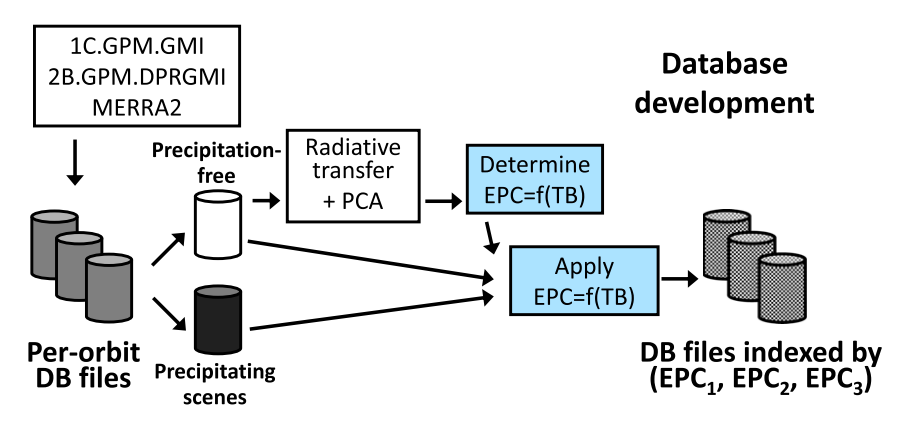


FIG. 1. Block diagram of the a priori database development for the EPC algorithm. A principal component analysis (PCA) uses the large collection of DPR precipitation-free observations to compute the coefficients that transfer the TB observations to EPC space (blue boxes) and index the a priori database by the first three EPC elements.

validating the full profile is that the 3D volumes sampled by scanning ground-based radars and space-based measurements are not aligned, and the ground radar scans do not fully capture the full top-to-bottom cloud structure. On the other hand, surface precipitation data are more widely collected and disseminated, e.g., the Ground Validation Multi-Radar Multi-Source (GV-MRMS) data in the United States (Kirstetter et al. 2012). Spaceborne radar observations are an exception, as these can provide the vertical structure of precipitation on a global scale. After the launch of the Tropical Rainfall Measuring Mission (TRMM) satellite, the TRMM Precipitation Radar (PR) and its successor, the GPM Dual-Frequency Precipitation Radar (DPR), have contributed to better understanding of the physics and characteristics of vertical structures of precipitation systems (Hirose and Nakamura 2004; Yamamoto et al. 2006; Liu and Zipser 2013; Kobayashi et al. 2018).

An improved depiction of the vertical precipitation profiles by the satellite observations also has potential to benefit the surface precipitation estimates. Based on TRMM PR observations, Utsumi et al. (2019) demonstrated that taking into account the precipitation vertical profile improves the satellite-based estimations of surface rain accumulation on subhourly time scales (e.g., 30 min). If passive MW retrievals can estimate precipitation vertical profiles in a reasonable accuracy, the method proposed by Utsumi et al. (2019) could be applicable to improving passive MW-based estimations of subhourly surface precipitation accumulation. Such a product could contribute to future improvements of merged satellite precipitation products (e.g., Huffman et al. 2018; Joyce and Xie 2011; Kubota et al. 2020) which provide subhourly precipitation estimates.

The objective of this study is to provide a comprehensive evaluation of the vertical precipitation profiles estimated by two radiometer algorithms, i.e., the version 5 GPROF and the emissivity principal components (EPC) technique developed by the authors. The GPM radar-radiometer (DPR + GMI) combined algorithm (2B-CMB) (Grecu et al. 2016) precipitation estimates, by virtue of collocation on the same GPM spacecraft, are used as a common profile reference. Sections 2 and 3 describe the data and methods used and a brief

description of each algorithm. Section 4 presents an evaluation of the surface precipitation rate by the passive MW algorithms, and sections 5–7 present evaluations of the vertical precipitation profiles. In section 8, the joint verification of the vertical precipitation profiles and the surface precipitation rate is presented. Section 9 is devoted to the discussion, and section 10 presents the summary and concluding remarks.

#### 2. Data

#### a. Emissivity principal components algorithm product

The EPC (Turk et al. 2018) algorithm is designed around the collection of the GPM Microwave Imager (GMI) observations coincident with DPR for precipitation-free conditions (Fig. 1). The precipitation-free condition is declared for each GMI field-of-view (FOV) pixel when any range bin of the DPR's normal scan (NS; Ku band) and matched scan (MS; Ka band) 3 × 3 radar reflectivity profiles surrounding the center of the GMI FOV do not exceed a sufficiently small threshold (15 dB). From the precipitation-free scenes inferred from the DPR profiles, together with the Modern-Era Retrospective Analysis for Research and Applications version 2 (MERRA-2) (Gelaro et al. 2017) temperature and water vapor profile, the surface emissivity for GMI's first nine (89 GHz and below) channels is estimated by the emissivity retrieval method of Mathew et al. (2008) with the successive order of interaction (SOI) radiative transfer model (Heidinger et al. 2006), regardless of the surface. For each precipitation-free pixel observation, the emissivity state vector is defined using the emissivity at these nine GMI channels and three corresponding environmental variables:

$$\mathbf{x} = (e^{10V}, e^{10H}, e^{18V}, e^{18H}, e^{23V}, e^{36V}, e^{36H}, e^{89V}, e^{89H}, \text{TQV}, T_s, T_{2m})^{\text{T}},$$
(1)

where  $\mathbf{x}$  is the emissivity state vector for a cloud-free pixel observation;  $e^c$  is the emissivity at a frequency channel c; and the TQV,  $T_s$ , and  $T_{2m}$  are the total column water vapor, surface temperature, and 2-m air temperature from MERRA-2,

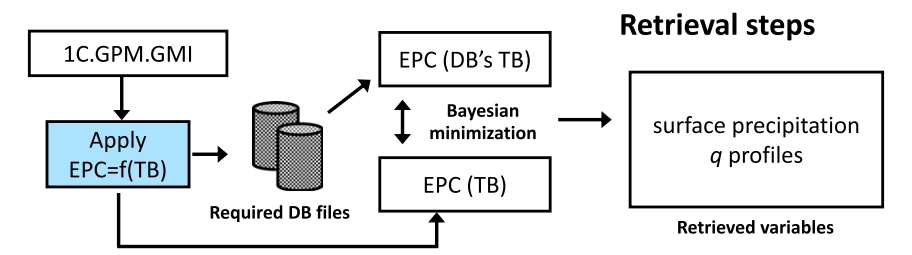


FIG. 2. Block diagram of the EPC constellation radiometer precipitation profile estimation technique. The EPC retrieval is similar to the facility GPROF algorithm, except that the observations and database entries are weighted in EPC space. The surface precipitation rate and condensed water content q profiles are estimated at the same time.

respectively. From the large set of the precipitation-free observations, we obtained a collection of the emissivity state vector, denoted **X**:

$$\mathbf{X} = \begin{bmatrix} e_{1}^{10V} & e_{n}^{10V} \\ e_{1}^{10H} & e_{n}^{10H} \\ \vdots & \vdots \\ e_{1}^{89H} & \cdots & e_{n}^{89H} \\ TQV_{1} & TQV_{n} \\ T_{s,1} & T_{s,n} \\ T_{2m,1} & T_{2m,n} \end{bmatrix}, \qquad (2)$$

where n is the number of the precipitation-free observations. Each emissivity state vector [i.e., each column of the right-hand side of the Eq. (2)] can be transformed into its 12 principal components via a transformation expressed by an orthogonal matrix, whose columns are the eigenvectors of the covariance matrix of  $\mathbf{X}$ .

The principal components of the emissivity state vector, or the EPCs, have nonlinear relationships with the observed TB (Turk et al. 2016). In the EPC algorithm, each EPC vector term is regressed against the nonlinear combination of the observed TB (the nonlinear TB combinations are included to represent the nonlinearities between emissivity and TB). For example, the first emissivity principal component element  $u_1$  is regressed as

$$u_{1}' = a_{0} + \sum_{k=1}^{13} b_{i} T_{B}^{i} + \sum_{i=1}^{13} \sum_{j=i}^{13} c_{ij} T_{B}^{i} T_{B}^{j} + \sum_{i=1}^{12} d_{i} \frac{(T_{B}^{i+1} - T_{B}^{i})}{(T_{B}^{i+1} + T_{B}^{i})}, \quad (3)$$

where  $u_1'$  is the regressed  $u_1$ ,  $T_B^i$  ( $i=1, 2, \ldots, 13$ ) are the GMI TBs at the 13 frequency channels (10V, 10H, ..., 183  $\pm$  7V),  $a_0$ ,  $b_i$ ,  $c_{ij}$ ,  $d_i$  ( $i=1,2,\ldots,13$ ; j=i,  $i+1,\ldots,13$ ) are the regression coefficients for the first emissivity principal component element. The other 11 elements of the emissivity principal components are regressed against TBs in the same way. This provides a transformation for computing the EPC vector directly from TB without a radiative transfer calculation. The correlation coefficient between the actual EPC and the estimated EPC exceeds 0.9 (not shown), suggesting that these EPC can be well represented by the GMI TB.

A separate a priori database is developed based on one year (January–December 2017) collection of GMI and the combined radar–radiometer algorithm product (2B.GPM.DPRGMI.

CORRA V06; Grecu et al. 2016) (CMB product hereafter) that includes both precipitation-free and precipitating scenes. For each GMI FOV pixel, the  $3 \times 3$  pixel average of the surface precipitation rate (variable name: "precipTotRate") and the condensed water content profiles (variable name: "precipTotWaterCont") at the normal scans from the CMB product are assigned. Other variables such as precipitation type from the CMB product, uncorrected radar reflectivity profile from the DPR-Ku product, and the environmental variables (TQV,  $T_s$ ,  $T_{2m}$ ) from MERRA-2 are also included in the database for analysis purposes. The a priori database is indexed by the first three EPC terms derived from Eq. (3). While the transformation for the TB into EPC [Eq. (3)] is specifically derived from the DPR noncloud TB scenes, it can be applied to all TB for discriminating the presence of precipitation affected scenes against the natural variability in the precipitationfree surface emissivity. There is no conceptual distinction made for the surface type, since all such distinctions are embedded in the transformation coefficients used for each a priori database. The EPC algorithm (Fig. 2) is based upon a Bayesian minimization between the observed EPC vector and the EPC vector from database candidate profiles. The EPC algorithm produces a Bayesian average of the near-surface precipitation rate and a Bayesian average of the corresponding condensed water content profile that best agrees with the TB observation in the Bayesian minimum-EPC distance sense (Fig. 2).

#### b. GPROF product

Another passive MW-based precipitation estimate investigated in this study is the GPM GPROF product for GMI (2AGPROFGMI V05; GPROF hereafter) distributed by the NASA's Precipitation Processing System (PPS). This product provides surface precipitation rate and vertical hydrometeor profiles estimated by the Goddard profiling algorithm (Kummerow et al. 2015).

Like the EPC, GPROF employs a Bayesian approach to estimate precipitation profiles and surface precipitation rate, but with a different database stratification and minimization scheme. GPROF for GMI uses an a priori database primarily built upon the precipitation profiles and surface precipitation estimated by the CMB and DPR-Ku products and their corresponding TBs observed by GMI for September 2014–August 2015 (Passive Microwave Algorithm Team Facility 2018). The major distinction between the EPC and GPROF is that GPROF uses ancillary information [i.e., total precipitable

water, 2-m temperature, and the land surface classification type derived from the Tool to Estimate Land Surface Emissivities at Microwave frequencies (TELSEM; Aires et al. 2011)] to subset the database, whereas the EPC is based on the emissivity structure and does not require any prior surface classification. Such technical difference in subsetting database may affect the retrievals particularly over complex surfaces with mixed emissivity structures (e.g., coast). GPROF estimates the surface precipitation rate and corresponding vertical precipitation profiles (hydrometeor content profiles) based on the Bayesian minimization of the observed TB and the TB from the a priori database, whereas EPC carries out its Bayesian minimization by comparing the observed EPC and the EPC from its a priori database.

The hydrometeor profiles provided by GPROF have five categories, i.e., rainwater, cloud water, ice water, snow water, and graupel and hail content. In this study, the total of the rainwater, ice water, and graupel and hail content is considered as the precipitation profile, or the condensed water content profile. The profiles are provided on the 500-m vertical resolution up to 10-km height and 1-km vertical resolution from 10- to 18-km heights. In this study, the profile layers above 10 km are simply divided to 500-m layers. Based on an analysis with the CMB product over land regions, the bottom of the lowest layers is considered to be at the actual surface height. Because GPROF does not estimate hydrometeor profiles over snow surfaces, the snow surface scenes are excluded from the analyses for the precipitation profiles for both GPROF and EPC.

#### c. Surface type information

While the EPC does not use the surface index, it is in the EPC database for analysis purposes, as a means to efficiently separate the results of this study by fixed surface types. The surface type information obtained from GPROF product provides 14 surface type classes (i.e., ocean, sea ice, five types of vegetation, four types of snow cover, standing water, land/ocean or water coast, and sea ice edge) based on self-similar emissivities derived from TELSEM (Aires et al. 2011; Passive Microwave Algorithm Team Facility 2018). In the analysis of this study, these surface types are regrouped into four types, i.e., ocean, vegetation (combined five vegetation types), snow cover (combined four snow cover types), and coast (land/ocean or water coast in the original surface type). Sea ice, standing water, and sea ice edge types are excluded in this study.

#### d. Reference datasets

Surface precipitation rate and precipitation water content profiles from passive MW algorithms are compared to those from the CMB product. The CMB product is based on the observations by the dual-frequency radar (DPR) and radiometer (GMI) carried on the GPM Core Observatory satellite. It is designed to provide the most accurate surface precipitation rate and vertical precipitation water content distribution. In this study, the surface precipitation rates (variable name: "precipTotRate") and vertical profiles of precipitation-size condensed water content (variable name: "precipTotWaterCont") at the NS from the CMB product

are used as the reference. Also, the freezing-level height and precipitation type information provided by this product is used in the analysis. The precipitation type of the CMB product is a copy from the GPM DPR Ku-band product. There are three categories in the precipitation type, i.e., stratiform precipitation, convective precipitation, and others, which are identified according to Awaka et al. (2016).

A ground-based surface precipitation rate over the continental United States and surrounding water by the Ground Validation Multi-Radar/Multi-Sensor (GV-MRMS) ground radar data, projected to the GMI footprints (Kirstetter et al. 2012, 2018), is also used for the validation of the surface precipitation rate. The precipitation rate by the GV-MRMS is available at the GMI footprints for each GPM *Core Observatory* satellite overpass.

#### 3. Evaluation method

The surface precipitation rates and the condensed water content profiles, or precipitation profiles, from the passive MW algorithms are investigated for 1000 granules of the GPM Core Observatory that are randomly sampled from a 1-yr period (June 2014–May 2015). This period was chosen based on the availability of EPC retrieval data. Note that it partially overlaps the period used for building GPROF's a priori database, and therefore GPROF's performance may be better in this period than in other period. Passive MW-based estimates are provided on GMI pixel locations (221 pixels/scan), whereas the reference data from the CMB product is provided at the DPR pixel locations. For each GMI pixel, the nearest CMB pixel on the same granule is searched. The FOV size of GMI pixel is relatively larger (approximately  $32 \,\mathrm{km} \times 19 \,\mathrm{km}$  at  $10 \,\mathrm{GHz}$  and  $7 \,\mathrm{km} \times 4 \,\mathrm{km}$  at 89 GHz) than that of the CMB pixel (approximately  $5 \text{ km} \times 5 \text{ km}$ ). To reduce the analysis uncertainty due to the footprint size difference, the variables from the CMB are averaged over  $3 \times 3$  pixels and matched up with the GMI pixel. For each pair of the CMB ( $3 \times 3$  average) and GMI pixels, the volumetric convective fraction is defined as follows:

volumetric convective fraction = 
$$P_{\text{conv}}/P_{\text{total}}$$
, (4)

where  $P_{\rm conv}$  and  $P_{\rm total}$  are convective and total surface precipitation rate by CMB product in the  $3\times3$  CMB pixels, respectively. If the volumetric convective fraction is greater than 0.5, the pair of the observation is classified as the convective type. The other cases are classified as the stratiform type. Most of the analyses in this study (section 6 and after) are focused on the precipitating pixels, where both the CMB product and the passive MW algorithm have surface precipitation rate no less than  $0.5 \, \mathrm{mm \, h}^{-1}$ .

To mitigate the off-nadir angle effect of the CMB product (where the surface clutter is manifested at low-level heights), the analysis is limited to the estimates where the corresponding CMB pixel is at the near-nadir angle bins (angle bin number 19–31). Also, the analysis for the precipitation water content profiles is limited to the range bins higher than 1 km above the actual surface. The condensed water content profiles from CMB product and EPC algorithm are available at 250-m vertical resolution while that of GPROF is at 500 m (below 10-km height). In this study, all the condensed water content profiles

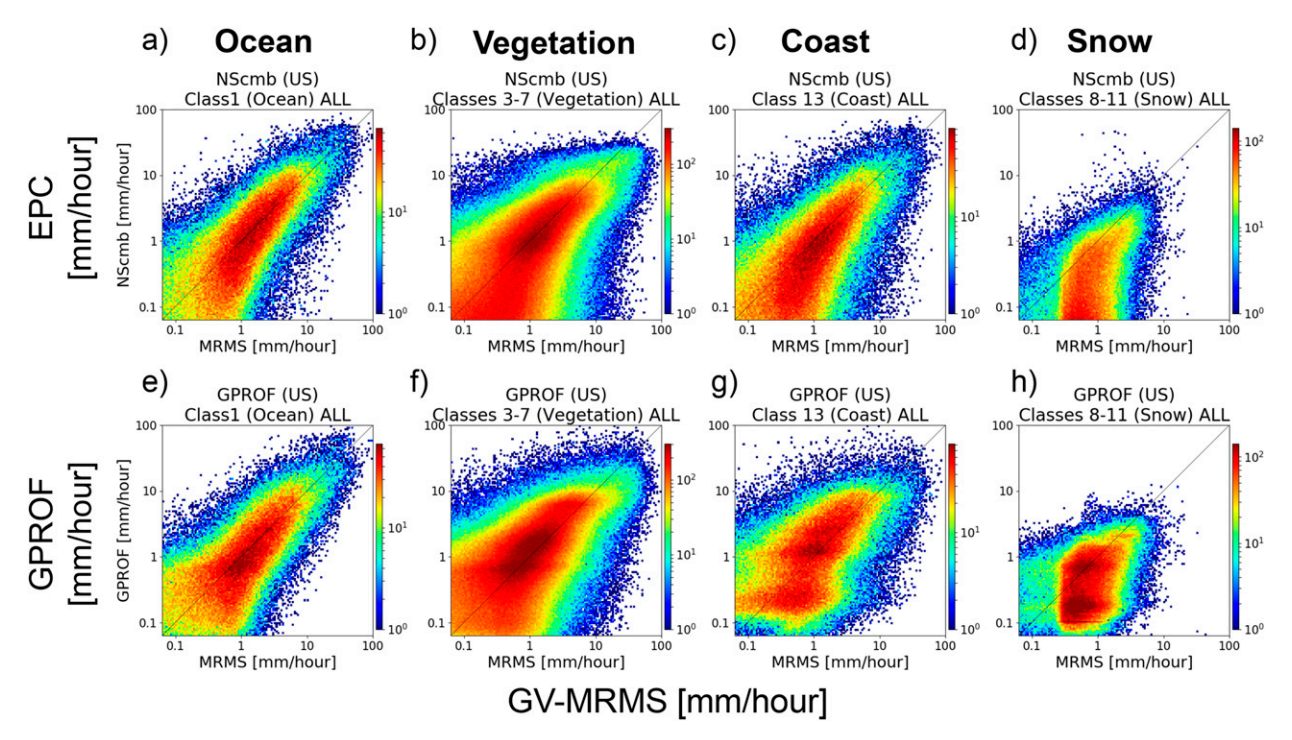


FIG. 3. Overall performance of the surface precipitation estimates by the passive microwave algorithms. The colors of the twodimensional histograms show the number of the cases. The estimations are validated with the GV-MRMS over the continental United States and surrounding water.

from CMB and EPC are averaged to 500-m vertical resolution for analysis.

### 4. Surface precipitation rate

Before looking into the precipitation vertical profiles, the surface precipitation rates from the two passive MW algorithms are examined. Figures 3 and 4 show comparisons of the surface precipitation rates with two different reference data (GV-MRMS and CMB product). Performance metrics of the passive MW algorithms computed with two different reference data are also summarized in Tables 1 and 2. Three performance metrics [i.e., root-mean-square error (RMSE), normalized mean bias, and correlation coefficient (CC)] are calculated as follows:

RMSE = 
$$\sqrt{\frac{\sum_{i}^{n} (y_i - x_i)^2}{n}}$$
, (5)

normalized mean bias = 
$$\frac{\frac{1}{n}\sum_{i}^{n}(y_{i}-x_{i})}{\frac{1}{n}\sum_{i}^{n}x_{i}},$$
 (6)

$$CC = \frac{\sum_{i}^{n} (x_i - \overline{x})(y_i - \overline{y})}{\sqrt{\sum_{i}^{n} (x_i - \overline{x})^2} \sqrt{\sum_{i}^{n} (y_i - \overline{y})^2}},$$
 (7)

where  $x_i$  and  $y_i$  are the surface precipitation rate of the reference and passive MW product, respectively, and  $\overline{x}$  and  $\overline{y}$  are the mean of each variable. The number of observations is n.

Although GPROF uses the GV-MRMS to build a priori database for the surface precipitation rate over snow surface, GV-MRMS is basically an independent data from the two passive MW algorithms. On the other hand, the CMB product is used to build a priori surface precipitation databases by EPC algorithm and GPROF (except for the snow surfaces for GPROF). In addition to the CMB product, GV-MRMS is also used as a reference dataset which enables validation against independent source. It is only used for the validation of surface precipitation over the continental United States because of its data availability, while the CMB product provides vertical profiles globally (60°S–60°N).

Figure 3 shows the validation of the two passive MW algorithms with GV-MRMS over the United States and surrounding water. In general, the two passive MW algorithms show reasonably good agreement with GV-MRMS, especially over ocean and vegetation surfaces. Over ocean, vegetation, and coast, EPC shows smaller RMSE and higher CC than GPROF (Table 1). Over snow surfaces, on the other hand, GPROF shows better RMSE and CC than EPC for some precipitation range. This could be because the GPROF uses GV-MRMS in its a priori database over snow surfaces. As for the normalized mean bias, the weak precipitation (0.1–1 mm h<sup>-1</sup>) tends to be underestimated by EPC over all surface types. One of the reasons of such underestimation could be attributed to the skewed probability distribution of the

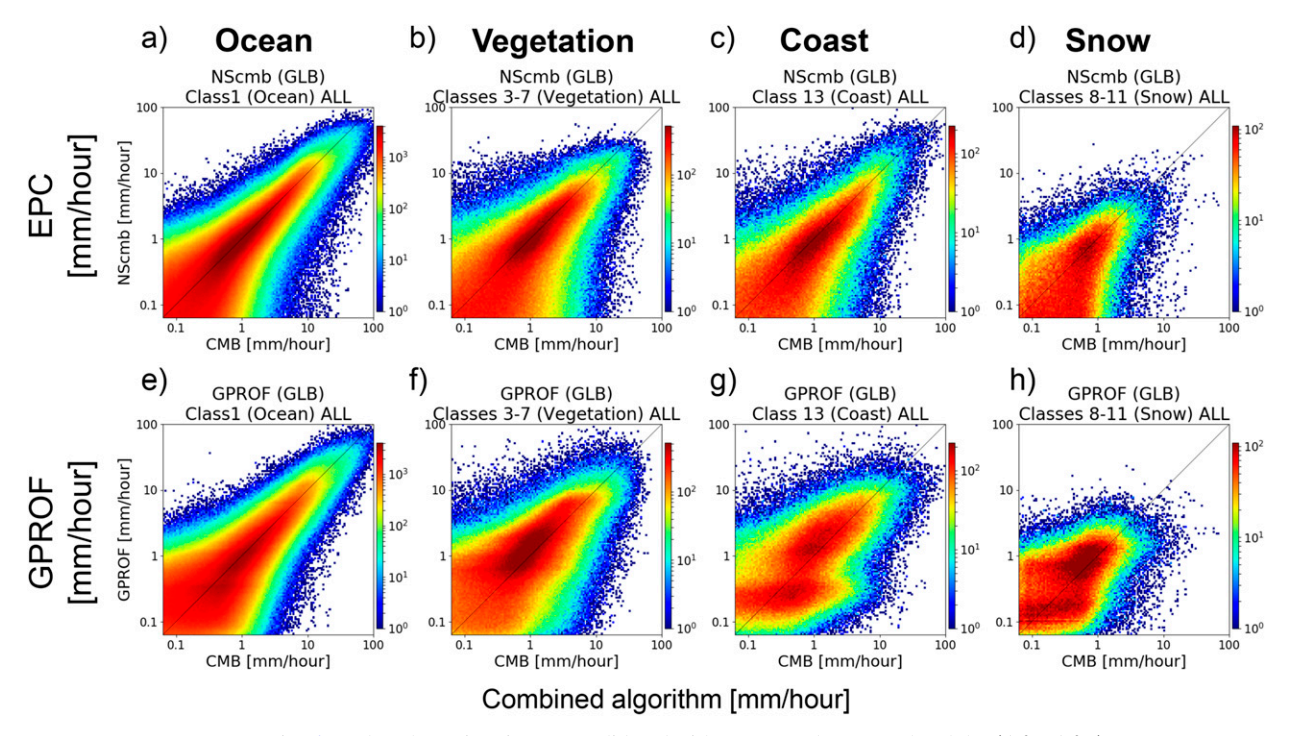


FIG. 4. As in Fig. 3, but the estimations are validated with CMB product over the globe (60°S-60°N).

precipitation rate in the a priori database, which can cause systematic biases of the Bayesian-type retrievals (Seo et al. 2007). Interestingly, on the other hand, GPROF shows overestimations for the same range  $(0.1-1 \text{ mm h}^{-1})$  except for snow surfaces (Table 1). The reason of the opposite biases of EPC and GPROF for weak precipitation range needs further investigation in the future study. Note that very light precipitation range (less than  $0.1 \,\mathrm{mm}\,\mathrm{h}^{-1}$ ) is not included in the assessment (Table 1). The performance evaluation for such very light range is more prone to the precipitation detection skill of the algorithms and the reference data, which is not the focus of this study. The heavy precipitation (more than 10 mm h<sup>-1</sup>) are generally underestimated by the two passive MW algorithms (Table 1), which is a known bias for both Bayesian and non-Bayesian type passive MW-based algorithms (e.g., Utsumi and Kim 2018). Over snow surfaces, the two passive MW algorithms generally underestimate the surface precipitation rate (Table 1), which could be due to a difficulty in separating TB signatures of precipitation against the background emissivity over snow surfaces (Liu and Seo 2013). GPROF shows bimodal features with peak occurrences around 0.3 and 1.0 mm h<sup>-1</sup> over coasts and around 0.2 and 1.0 mm h<sup>-1</sup> over snow surfaces (Fig. 3h). Similar bimodal features by GPROF are reported for the retrievals from the sounders [i.e., Advanced Technology Microwave Sounder (ATMS) and Microwave Humidity Sounder (MHS)] over ocean (You et al. 2020), although it remains to be clarified if they are rooted in the same causes. Such bimodal features are not apparent for the EPC algorithm.

Figure 4 shows the validation of the two passive MW algorithms with the CMB product over the globe (60°S–60°N). It shows similar results to the GV-MRMS case although the overall performances of the passive MW algorithms are better when they are validated with the CMB product (Fig. 4 and

Table 1. Performance metrics of the passive MW algorithms relative to GV-MRMS product. Metrics are shown for different precipitation ranges defined by the reference (GV-MRMS) product.

			RM	SE		N	Vormalized	CC					
Range $(mm h^{-1})$		≥0.1	0.1-1	1–10	≥10	≥0.1	0.1-1	1–10	≥10	≥0.1	0.1-1	1–10	≥10
Ocean	EPC	3.1	0.8	3.1	12.7	-0.04	-0.09	0.08	-0.25	0.70	0.25	0.53	0.41
	GPROF	3.2	0.8	3.3	12.8	-0.02	0.02	0.08	-0.21	0.71	0.23	0.51	0.43
Vegetation	EPC	2.8	0.8	2.6	15.1	-0.35	-0.15	-0.28	-0.58	0.61	0.21	0.41	0.34
_	GPROF	3.0	1.0	2.9	15.4	-0.15	0.26	-0.07	-0.56	0.56	0.22	0.39	0.28
Coast	EPC	2.8	0.8	3.0	14.0	-0.28	-0.26	-0.20	-0.46	0.61	0.20	0.44	0.32
	GPROF	3.1	1.4	3.2	14.6	-0.12	0.27	-0.03	-0.56	0.50	0.17	0.36	0.24
Snow	EPC	1.0	0.5	1.7	17.9	-0.77	-0.80	-0.74	-0.87	0.42	0.14	0.38	-0.03
	GPROF	0.9	0.5	1.5	18.2	-0.56	-0.49	-0.62	-0.90	0.41	0.16	0.39	-0.23

-													
			RM	SE		Normalized mean bias				CC			
Range $(mm h^{-1})$		≥0.1	0.1-1	1–10	≥10	≥0.1	0.1–1	1–10	≥10	≥0.1	0.1–1	1–10	≥10
Ocean	EPC	1.4	0.3	1.5	10.0	-0.13	-0.14	-0.09	-0.25	0.85	0.51	0.77	0.56
	GPROF	1.4	0.4	1.6	9.1	-0.14	-0.17	-0.10	-0.20	0.86	0.40	0.74	0.64
Vegetation	EPC	1.8	0.6	2.1	10.6	-0.34	-0.23	-0.33	-0.49	0.69	0.29	0.52	0.33
	GPROF	2.0	0.7	2.4	10.9	-0.08	0.26	-0.09	-0.42	0.64	0.32	0.46	0.28
Coast	EPC	1.9	0.6	2.3	11.4	-0.26	-0.19	-0.26	-0.31	0.72	0.30	0.54	0.44
	GPROF	2.3	0.9	2.6	13.3	-0.12	0.21	-0.11	-0.54	0.56	0.29	0.41	0.22
Snow	EPC	0.8	0.4	1.6	15.1	-0.51	-0.52	-0.47	-0.79	0.49	0.32	0.32	0.11
	GPROF	0.8	0.5	1.6	16.2	-0.27	-0.14	-0.42	-0.89	0.37	0.34	0.16	0.07

TABLE 2. As in Table 1, but relative to CMB product.

Table 2). Since both two passive MW algorithms use the CMB product for their a priori databases, it is reasonable that they inherit the nature of the CMB product and agree with it better than GV-MRMS. A noticeable difference from the GV-MRMS case is found over snow surfaces, where a cutoff pattern around  $0.3 \, \text{mm h}^{-1}$  is inconspicuous for the CMB case. Part of the differences in the evaluation results could be due to the difference in the threshold or sensitivity of the reference data at the lowest precipitation rate, as well as the different spatial extent of the validation data (i.e., over the United States in Fig. 3 and over the globe in Fig. 4).

We note that GV-MRMS does not provide the associated vertical structure of the precipitation profiles. In the following sections, the CMB product is used as the reference dataset.

#### 5. Example case of the retrieved profiles

On 14 October 2014, the GPM *Core Observatory* satellite observed a frontal precipitation over the eastern United States. The northern part of the precipitation band is over land and the rest is over ocean (Gulf of Mexico) (Fig. 5). Figure 6 shows the vertical cross section of the radar reflectivity (uncorrected for attenuation) measured by DPR–Ku (Fig. 6a) as well as the estimated radar reflectivity by EPC algorithm (Fig. 6b). The a priori database of EPC algorithm contains "uncorrected" radar reflectivity taken from DPR–Ku product for analysis purpose. Since the Bayesian average of the radar reflectivity is not output of the EPC algorithm, the radar reflectivity of the a priori database entries that are assigned the highest weight in the Bayesian retrieval, which we call the "top-weighted profile," are used as the estimated profile of the reflectivity.

The radar reflectivity signals are well reconstructed by the EPC algorithm. The reconstructed reflectivity profile estimated by EPC algorithm shows the locations of the strong precipitation signals and the precipitation top heights are very similar to the radar observation, although there are some second-order discrepancies such as bright band signals observed by DPR-Ku (between pixel number 60 and 80) and a missing signature near the convection (pixel number 12). The anvil-like structure in the south over ocean (around pixel number 3–4) is also reconstructed. This implies that the EPC passive MW algorithm has skill in representing the precipitation profiles depicted by the observed radar reflectivity.

Figure 7 shows the precipitation condensed water content (condensed water content, hereafter) profiles from the CMB product, EPC algorithm, and GPROF. The similarities between the CMB algorithm product and the passive MW-based estimates are not as notable as that of the radar reflectivity profile. The EPC algorithm tends to underestimate the condensed water content. Also, a precipitating column near the strong convection (pixel number 12) is not reproduced in this case. GPROF tends to show strong signatures that spread wider both vertically and horizontally in space. Despite these biases, the main features of this scene, e.g., the tall precipitation around pixel number 9-12 and the precipitation system around pixel number 70-90 with peaks of condensed water content at 4-5.5 km, are reasonably represented by both passive MW algorithms. It suggests that the precipitation water content profiles can also be estimated by passive MW algorithms, even over land surfaces, with some biases.

#### 6. Average profiles of condensed water content

Figure 8 presents the average precipitation water content profiles over two surface types (ocean, vegetation) for convective and stratiform precipitation. The bottom of the profiles corresponds to the actual surface height. The analysis hereafter is confined to the precipitating pixels.

Since we have found in a preliminary investigation that the freezing level height largely affects the shape of the condensed water content profiles, the analysis is conditioned on the typical freezing level heights as well as latitude bands, i.e., (i) the middle-to-high latitudes (35°–60°S and N) with the freezing level conditioned on 0–1 km from the surface, which represent the cold season cases, (ii) the middle-to-high latitudes with the freezing level conditioned on 3–4 km, which represent the warm season cases, and (iii) the tropics (15°S–15°N) with the freezing level conditioned on a typical range in the tropics (4–5 km).

The consistency of the passive MW-based profiles with the reference data largely varies among different conditions. For example, the average profile of the stratiform precipitation over the ocean in the tropics estimated by EPC (Fig. 8i) is almost identical to the reference data. On the other hand, the average profile of the cold season convective precipitation in the middle-to-high latitudes over ocean (Fig. 8c) is better estimated by GPROF. In the following subsections, the passive

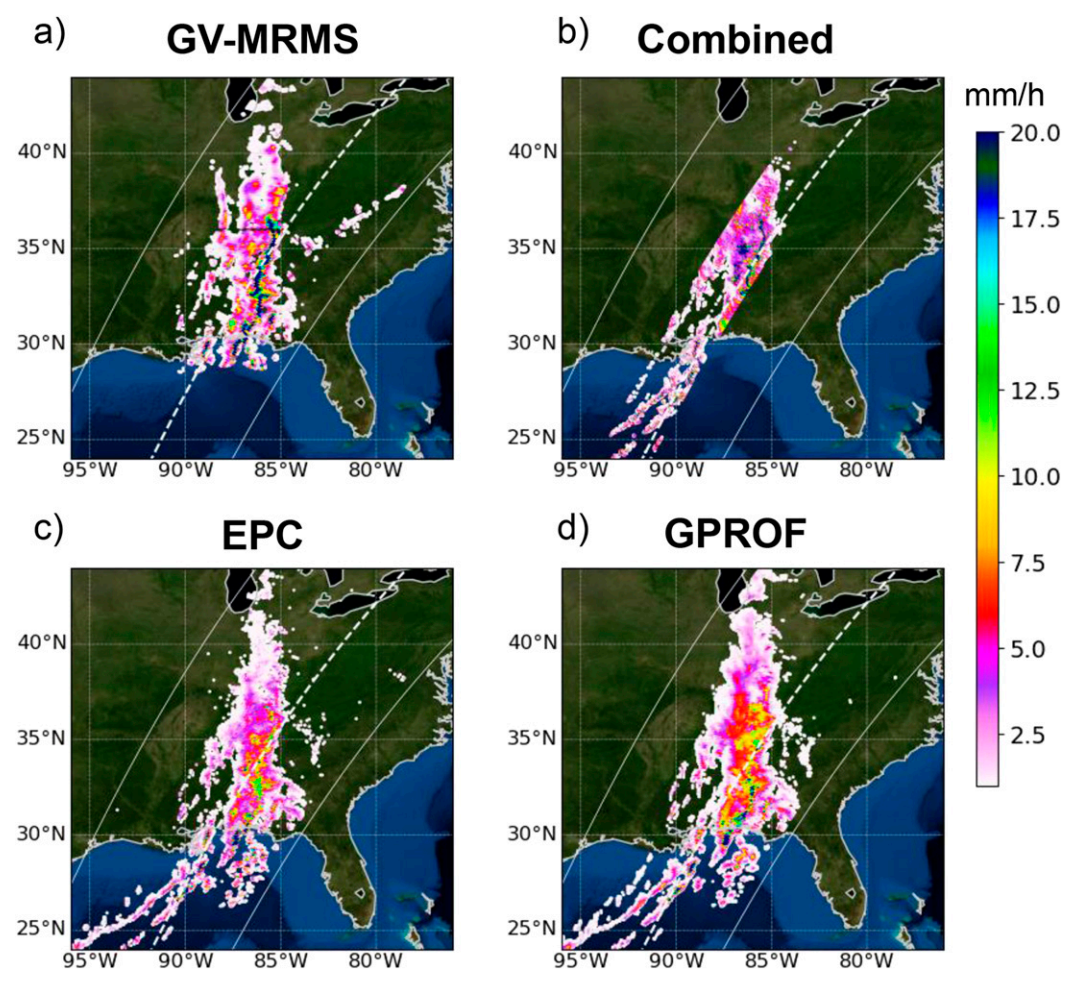


FIG. 5. Surface precipitation estimates for a frontal precipitation case on 14 Oct 2014, over the southeastern United States (GMI granule number 3556). Only the pixels with precipitation rate no less than  $0.5 \text{ mm h}^{-1}$  are shown. The parallel white solid lines show the boundaries of the GMI swath, and the white dashed line in between them is the location of the cross section for Figs. 6 and 7.

MW-based profiles are investigated from two aspects, i.e., the magnitude (section 6a) and the shape (section 6b).

#### a. Magnitude

To investigate the magnitude of the profiles, the condensed water content at the peak heights of the profiles is examined. Here, the peak heights are defined as the heights (above 1 km) where the profile shows the largest condensed water content. In general, the EPC algorithm tends to underestimate the condensed water content of the convective precipitation (e.g., Figs. 8c,d,g,h,k,l). On the other hand, the profile magnitude of the stratiform precipitation is well reproduced by EPC when freezing level height is not very low (e.g., Figs. 8e,f,i,j).

GPROF systematically overestimates the magnitude of the condensed water content profiles for stratiform precipitation. In the tropics over the ocean, the average magnitude of the stratiform cases (Fig. 8i) is even larger than the convective cases (Fig. 8k). For convective precipitation, GPROF shows both underestimations (e.g., Fig. 8g) and overestimations

(e.g., Fig. 8k) for the magnitude of the profiles depending on the condition.

Although the CMB product is used as a reference dataset, it is noteworthy that the CMB product also can be affected by some algorithmic shortcomings. For example, CMB product tends to show larger surface precipitation rate over land compared to other global precipitation products (Skofronick-Jackson et al. 2017), which may affect the vertical profiles. Also, CMB product may be missing high-latitude oceanic drizzle and snowfall over land due to the DPR sensitivity (Passive Microwave Algorithm Team Facility 2018). GPROF addresses this potential missing problem of the CMB product by adjusting the hydrometeor profiles. This may be one of the reasons of the different magnitudes between GPROF and CMB product for middle-to-highlatitude stratiform precipitation (Figs. 8a,b,e). However, such potential missing problem of the CMB product does not apply to the tropics. Also, the very light precipitation cases are excluded in the current analysis (see section 3), and it should mitigate the potential missing effect of the CMB in this comparison.

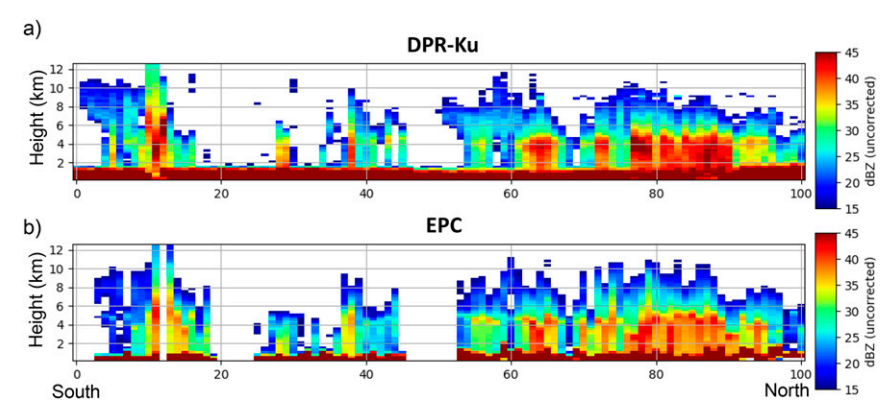


FIG. 6. Vertical cross section of the radar reflectivity. (a) Observed by DPR-Ku. (b) Topweighted profiles in the EPC algorithm's Bayesian retrieval (see the text).

#### b. Shape

Figure 8 suggests that the shape of the mean condensed water content profiles can be abstracted by the position of the peak heights (which is defined earlier) of the profiles. In general, the two passive MW algorithms capture the shapes of the mean condensed water content profiles with small biases of the peak height (±1-km range). It is evident from the profiles of the CMB product that the mean peak height is located near the freezing level height. This is reasonable considering that the phase change from snowflakes to raindrops around the freezing level increases the falling velocity of the precipitation particles. The faster falling velocity of the raindrops leads to the rapid decrease in the condensed water content below the freezing level. This reasoning could be especially valid for stratiform precipitation, but a similar pattern is found for convective precipitation as well (Fig. 8). This result means that the two passive MW algorithms capture the average shape of the condensed water content both in the ice (i.e., above freezing level) and liquid (i.e., below freezing level) phases. Also, this result implies that the explicit consideration of the freezing level height may further improve the representation of the shapes of the condensed water content profiles by the passive MW algorithms.

In this section, it is found that the passive MW algorithms have magnitude biases for the condensed water content profiles while they can represent the average shapes of the profiles reasonably for typical precipitating cases. The potential causes of the magnitude bias are further discussed in section 9.

#### 7. Global pattern of the retrieval performance

Three metrics of the condensed water content profiles (mean condensed water content, storm top height, and correlation coefficients of the profiles between the CMB product and passive MW algorithms) are investigated in sections 7a, 7b, and 7c, respectively. The condensed water content profiles of the CMB and passive MW products are paired at all

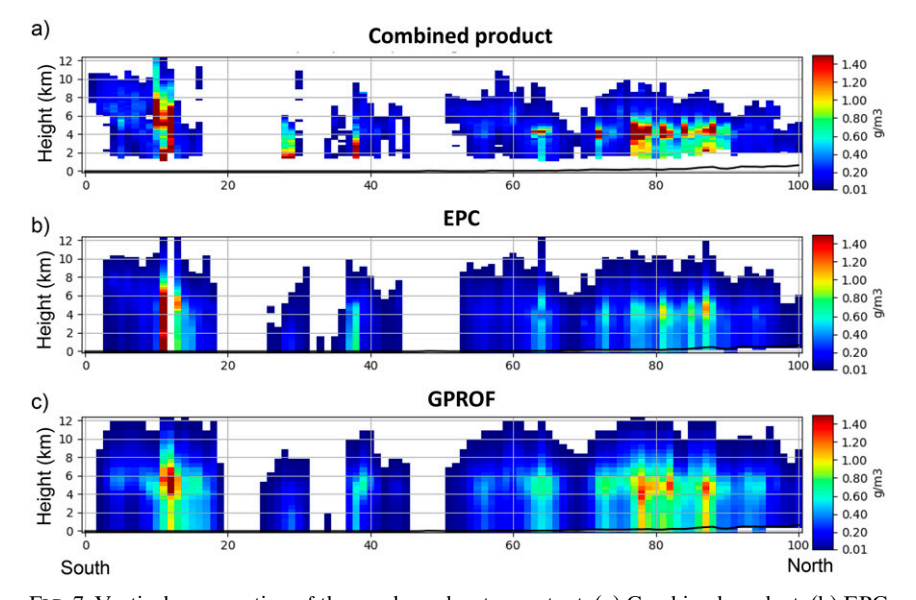


FIG. 7. Vertical cross section of the condensed water content. (a) Combined product. (b) EPC algorithm. (c) GPROF.

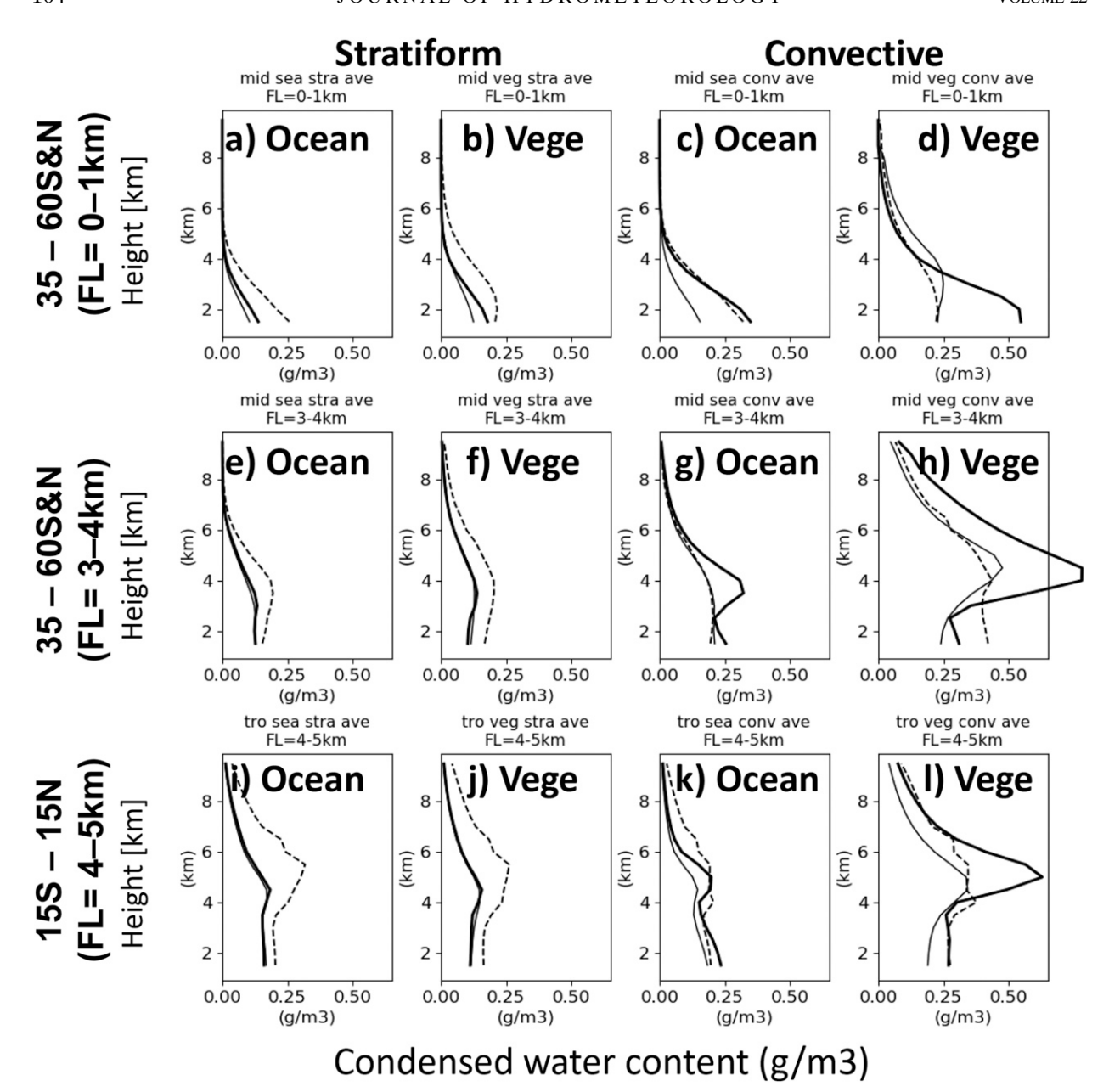


FIG. 8. Average vertical profiles of the condensed water content over ocean (Ocean) and vegetation (Vege). (a)–(d) The cases of freezing level = 0-1 km in  $35^{\circ}$ – $60^{\circ}$ N and S. (e)–(h) The cases of freezing level = 3-4 km in  $35^{\circ}$ – $60^{\circ}$ N and S. (i)–(l) The cases of freezing level = 4-5 km in  $15^{\circ}$ S– $15^{\circ}$ N. Thick sold lines: Combined product. Thin sold lines: EPC algorithm. Dashed lines: GPROF.

precipitating pixels (i.e., pixels with surface precipitation rate no less than  $0.5\,\mathrm{mm\,h^{-1}}$  in both products). The metrics and their difference between the CMB and passive MW products are calculated for each pair of the profiles and the average and the standard deviation of the metrics are calculated for  $2.5^{\circ} \times 2.5^{\circ}$  grid boxes globally ( $60^{\circ}\mathrm{S}-60^{\circ}\mathrm{N}$ ).

#### a. Mean condensed water content

Figure 9 shows the global pattern of the mean condensed water content (units of g m<sup>-3</sup>), which is a metric of the magnitude of the precipitation profiles. This metric is calculated by

averaging the condensed water content between 1 and 10 km from the surface for each profile. Some profile data in the investigated products have layers with missing value. The layers with the missing value are not used in the averaging. We used the average (instead of total) of the condensed water content for this analysis to avoid the negative bias due to the missing data in the profiles. In the vertical averaging, we assume that such missing happens randomly, which does not likely cause systematic bias. The difference of the metrics between CMB and passive MW products is normalized by the mean condensed water content of the CMB product for each observation.

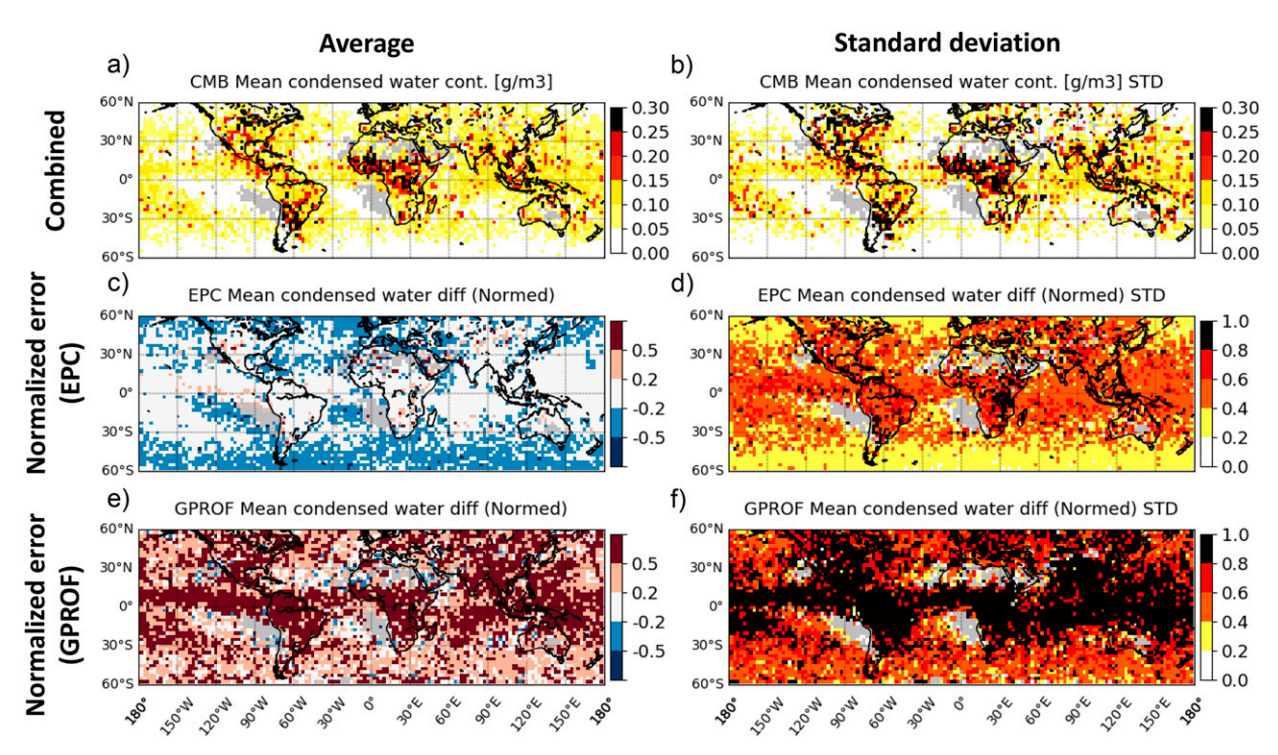


FIG. 9. Mean condensed water content. (a),(b) Combined product. (c)–(f) Normalized errors of the mean condensed water content by the passive microwave algorithms. Left and right columns are the average and the standard deviation of the metrics. Gray color indicates a location where no precipitation case is available.

As expected, the mean condensed water content (Fig. 9a) has a similar global pattern to the surface precipitation rate, although the land regions show higher mean condensed water content than the ocean. A separate analysis for the condensed water content at the peak height of the profiles (not shown) shows a similar global pattern, which further confirms that the magnitude of the precipitation profiles tends to be larger over land than ocean.

The two passive MW algorithms show different global patterns of the biases. The bias of EPC tends to be larger in the middle-to-high latitudes while that of GPROF is larger in low latitudes (Figs. 9c,e). On average, EPC shows 20%-50% underestimation in the middle-to-high latitudes. In the low latitudes, the EPC represents the profile magnitude reasonably well. Although the average profile analysis of Fig. 8 suggests the EPC's underestimation of the profile magnitude for the tropical convective precipitation, the average bias does not exceed -20% in most of the tropics (Fig. 9c). GPROF shows relatively larger bias in the profile magnitude. It has more than 50% overestimation in the low latitudes and some land regions in the middle latitudes, as well as 20%-50% overestimation in the large part of the middle-to-high latitudes. It is interesting that GPROF generally overestimates mean condensed water content while the surface precipitation rate tends to be slightly underestimated (Tables 1 and 2). One of the reasons of the larger profile magnitude could be due to the adjustment done for the profiles in the GPROF a priori database (Passive Microwave Algorithm Team Facility 2018; Ringerud et al. 2019).

The standard deviation of the normalized difference shows the variability of the algorithms' performance for estimating the profile magnitude (Figs. 9d,f). In general, EPC shows smaller standard deviations of the normalized difference than GPROF. Both passive MW algorithms have relatively higher standard deviation of the normalized difference in the low latitudes, which means that the agreement of the profile magnitude between the CMB and passive MW products for each observation is highly variable in the region. It reflects the difficulty in capturing the large spatiotemporal variability of the precipitation system in the low latitudes.

#### b. Storm top height

The storm top height (Fig. 10), or the precipitation top height, is one of the properties that characterize the vertical structure of the precipitation. The CMB product provides the storm top height variable (i.e., variable name "stormTopAltitude"), which is defined as the height of the highest range bin where the significant DPR-Ku radar echoes are observed at least three consecutive bins. On the other hand, the passive MW algorithms do not provide storm top height as a standard output variable. In this study, the storm top height is defined as the height (relative to the surface) of the highest profile layer where the condensed water content exceeds a threshold (0.033 g m<sup>-3</sup>). This threshold is the average of the condensed water content of the CMB product  $(3 \times 3 \text{ pixel averaged})$  at the height of the "stormTopAltitude." The storm top height analyzed in this study is defined using this threshold by applying it to each of the condensed water content profiles of the three products (CMB, EPC, and GPROF).

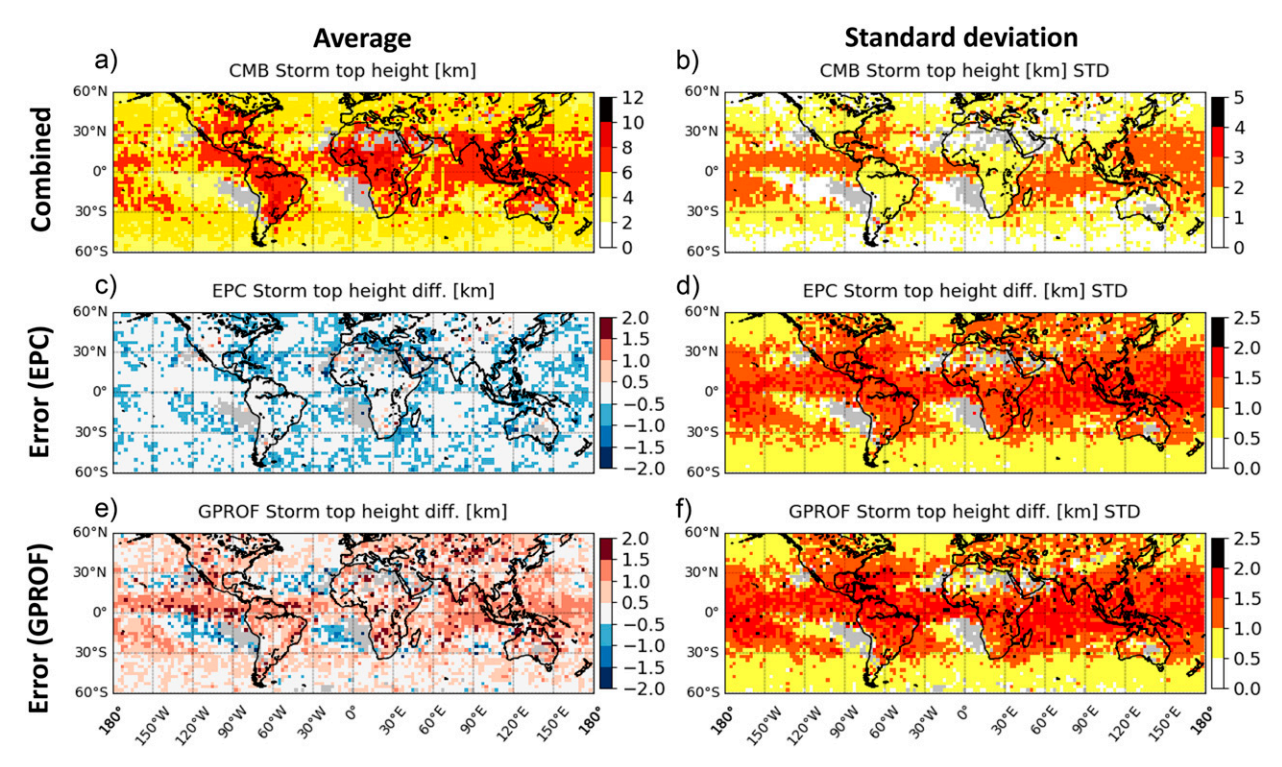


FIG. 10. Storm top height. (a),(b) Combined product. (c)–(f) Error of the storm top heights by the passive microwave algorithms. Left and right columns are the average and the standard deviation of the metrics. Gray color indicates a location where no precipitation case is available.

The storm top height by EPC is unbiased over most of the regions with some patchy underestimation biases of 0.5–1 km (Fig. 10c). GPROF has systematic overestimation bias of  $\sim\!0.5$ –1 km in the middle-to-high latitudes (Fig. 10e). It also shows overestimation bias of  $\sim\!1$ –1.5 km in the low latitudes as well as some land regions in the middle latitudes (Fig. 10e). These biases can be related to the bias of the magnitude of the profiles (Fig. 9). The standard deviations of the storm top height difference show similar global patterns for the two passive MW algorithms. The variability of the storm top height error, measured by one standard deviation, is  $\sim\!\!2\,\mathrm{km}$  in the low latitudes and  $\sim\!\!0.5$ –1 km in the middle and high latitudes.

#### c. Similarity of the profile shapes

The similarity of the profile shapes between the CMB and passive MW products is evaluated by the correlation coefficient of the profiles (Fig. 11):

CC of the profile shape 
$$= \frac{\sum_{i}^{n} (x_i - \overline{x})(y_i - \overline{y})}{\sqrt{\sum_{i}^{n} (x_i - \overline{x})^2} \sqrt{\sum_{i}^{n} (y_i - \overline{y})^2}}, \quad (8)$$

where  $x_i$  and  $y_i$  are the mean condensed water content at the *i*th vertical bin of the profile of the CMB and passive MW product, respectively;  $\bar{x}$  and  $\bar{y}$  are the vertically averaged mean condensed water content; and n is the number of 500-m vertical layers. Since the majority of the condensed water content is

found below ~7 km in most cases (cf. Fig. 8), the CC calculation is confined to the layers between 1- and 7.5-km height (from the surface) in order to better capture the shape similarity of the condensed water content profiles. The higher CC means the larger similarity of the profile shapes, regardless of magnitude biases. Note that the mean and the standard deviation of the CC is based on the CC computed for each pair of the profiles at the precipitating GMI pixel.

In general, EPC shows a higher average CC than GPROF (Fig. 11). As for the geographical pattern, the two passive MW algorithms' average performances for the profile shape are better in the middle-to-high latitudes over ocean (CC = 0.8 and higher) than in the low latitudes and land regions (CC = 0.4–0.8 for the EPC and CC = 0.2–0.8 for the GPROF) (Fig. 11). The standard deviation of the CC, the metric for the variability of the estimation performance, is higher in the low latitudes (Figs. 10b,d). For a given latitude, the land regions tend to have lower CC than the ocean, implying that the estimation of the profile shape is more difficult over land. This difficulty is due to the weak contrast of the precipitation and background signals in the passive MW observations over land.

## 8. Relationships between the errors in surface precipitation rate and profiles

As mentioned in section 1, the surface precipitation rate is physically related to the structure of the condensed water content profile through the mass transport. A physically

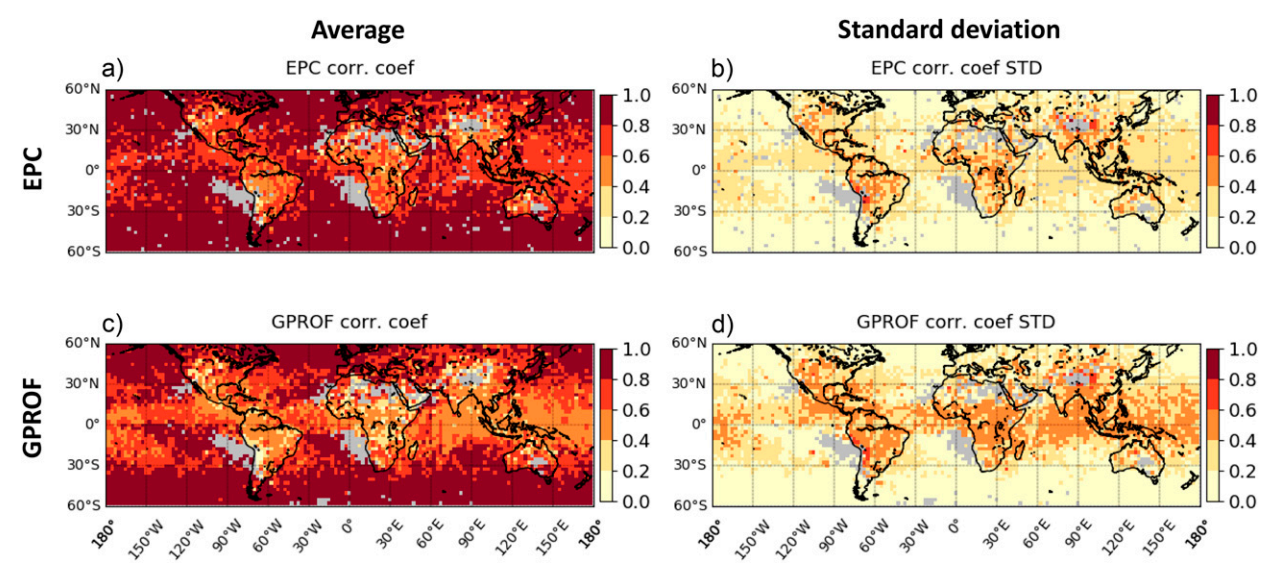


FIG. 11. Correlation coefficient of the condensed water content profiles between the combined product and passive microwave products. (a),(b) EPC algorithm. (c),(d) GPROF. Left and right columns are the average and the standard deviation of the metrics. Gray color indicates a location where no precipitation case is available.

complete passive MW retrieval should therefore attempt to estimate these two quantities jointly. This is also an implicit assumption in the passive MW algorithms for surface precipitation retrieval, since the microwave signals are more related to the hydrometeor content structure rather than to the precipitation rate at the ground surface. In this section, the joint analyses of the errors in surface precipitation rate and condensed water content profiles are presented.

Figure 12 shows the joint histogram of the surface precipitation rate error and two types of the profile metrics (i.e., normalized error of the mean condensed water content and the CC of the profile shapes). The errors in the surface precipitation rate and the mean condensed water content are normalized as follows:

normalized error of the surface precipitation=
$$\frac{(P_{\text{pmw}} - P_{\text{cmb}})}{P_{\text{cmb}}},$$

normalized error of the mean condensed water content

$$= \frac{(W_{\mathrm{pmw}} - W_{\mathrm{cmb}})}{W_{\mathrm{cmb}}},$$

(10)

where P and W are the surface precipitation rate and mean condensed water content of each precipitating scan pixel, respectively, and pmw and cmb mean the passive MW algorithm and the CMB product, respectively. The normalized error of the mean condensed water content is the same metric that was investigated in section 7a.

The errors in the surface precipitation rate and the mean condensed water content are positively correlated (Figs. 12a,c). Although there are some biases for the mean condensed water content (negative bias for EPC and positive bias for GPROF),

the smaller error in the surface precipitation rate tends to be accompanied by the smaller error in the mean condensed water content. This implies that there is a dependency between the retrieval performances of surface precipitation rate and the corresponding precipitation profile magnitude for the passive MW algorithms. The profile CC (Figs. 12b,d) also shows a certain relationship with the surface precipitation error. The cases with smaller error in the surface precipitation tend to be accompanied by higher profile correlation coefficient. This implies, although the relationship is not as distinct as the mean condensed water content, the better estimation of the surface precipitation has more chance to be accompanied by a better estimation of the associated profile shape.

The relationship between the error in the surface precipitation rate and the profile metrics found in this analysis suggests that the estimation of the surface precipitation rates and the vertical precipitation profiles are physically connected to each other. Also, it suggests that a good estimation of the surface precipitation rate by passive MW algorithms is physically reasonable in terms of its accompanying precipitation vertical profile too.

#### 9. Discussion

It was found in section 8 that the profile magnitude, measured by the mean condensed water content, is related to the surface precipitation estimates. However, the passive MW algorithms exhibit nonnegligible bias of the profile magnitude; i.e., underestimation by the EPC in the middle-to-high latitudes, and overestimation by GPROF over most of the global regions (Fig. 9). The biases in the profile magnitude is discussed in this section.

Figures 13a-d compare the mean condensed water content of the three products for the middle-to-high-latitude regions (35°-60°N and S) and the tropics (15°S-15°N). They are

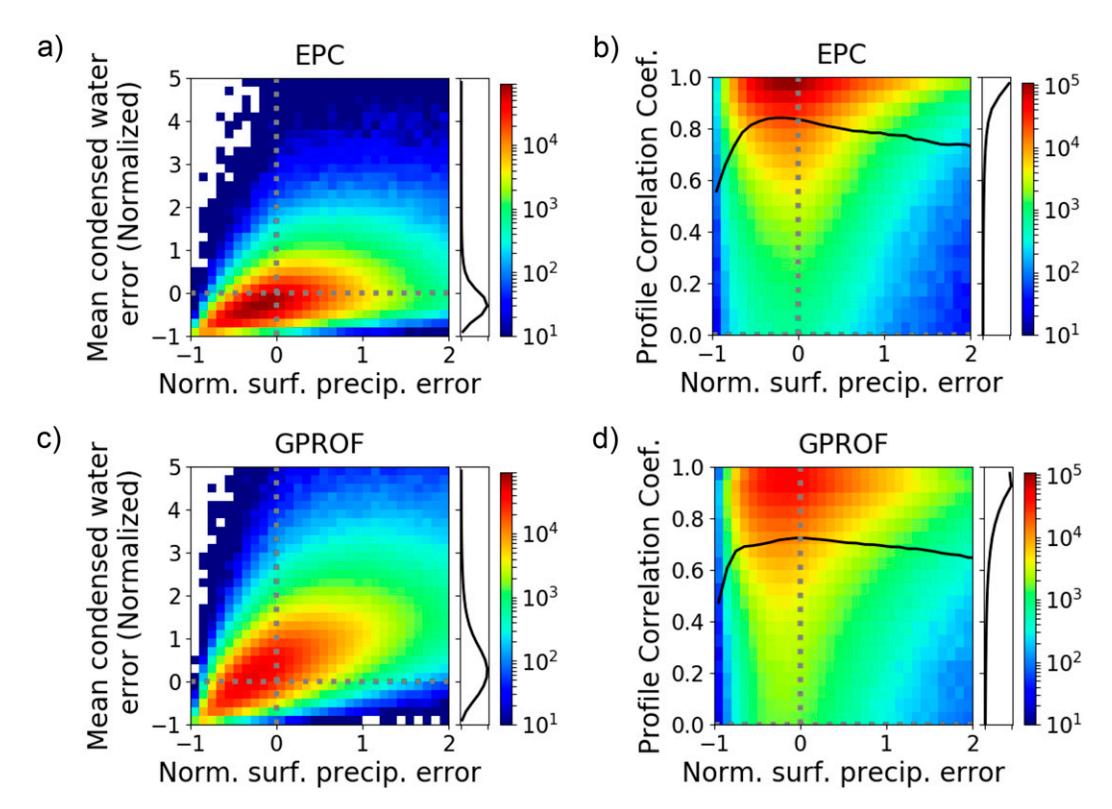


FIG. 12. Joint histograms of the metrics. (a),(c) Normalized surface precipitation error and normalized condensed water content error. (b),(d) Normalized surface precipitation error and correlation coefficient between condensed water content profiles. Black lines in (b) and (d) are the average of the profile correlation coefficients. The color shows the number of cases. The histograms of the metric along the vertical axis are also shown on the right side of each panel.

classified by the precipitation type (convective and stratiform) of the corresponding CMB product. EPC underestimates the mean condensed water content of the convective precipitation in both regions (-37% in the middle-to-high latitudes and -28% in the tropics) (Figs. 13a,c) and the middle-to-high-latitude stratiform precipitation ( $\sim$ -23%) (Fig. 13b). Considering the result of the average profile analysis of Fig. 8, the underestimation for the middle-to-high-latitude stratiform is mostly attributed to the bias for the cold season cases (see Figs. 8a,b). On the other hand, GPROF shows substantial overestimation of the mean condensed water content of the stratiform precipitation in both regions (+42% in the middle-to-high latitudes and +63% in the tropics) (Figs. 13b,d). Here, it is hypothesized that the bias in the precipitation type represented in the passive MW retrieval is one of the sources of the total bias.

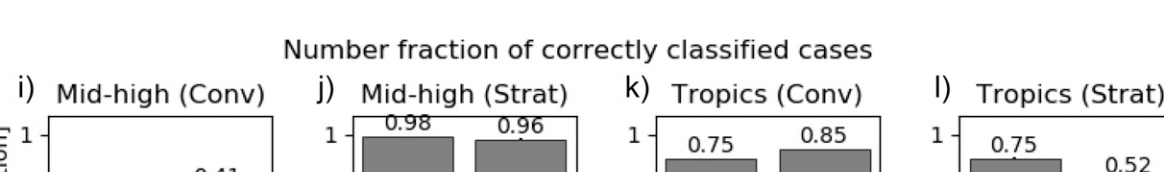
Both passive MW algorithms provide the convective surface precipitation rate as a standard output. In the same way as the precipitation type classification based on the CMB product (see section 3 for the method), the precipitation type can be defined using the volumetric convective fraction based on the passive MW algorithms. For the convenience of the discussion, the precipitation type based on the CMB product is called the "true" precipitation type hereafter.

Figures 13e-h compare the mean condensed water content for the cases where both CMB and passive MW products show the same precipitation type. They are, in other words, the cases

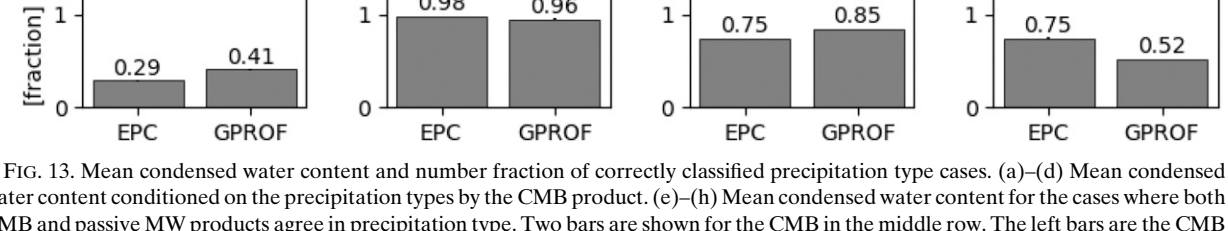
where the passive MW products successfully represent the true precipitation type. For the EPC algorithm, the noticeable negative bias for the middle-to-high-latitude convective profile magnitude that is found in Fig. 13a is largely reduced (from -37% to -25%; Figs. 13a,e), implying that the EPC's convective profile magnitude is less biased if the algorithm correctly identifies the precipitation type. This suggests that a substantial part of the EPC's underestimation bias found for the middle-to-high-latitude convective profile magnitude is due to the error in the precipitation type represented by the EPC algorithm. In fact, only 29% of the true convective events are correctly classified as the convective type by the EPC algorithm in the region (Fig. 13i). The contamination of the stratiform precipitation entries, which have generally smaller mean condensed water content, in the Bayesian retrieval can lead to the negative bias. Meanwhile, in the tropics, the underestimation bias of the convective mean condensed water content by EPC algorithm is only slightly reduced (from -28% to -25%; Figs. 13c,g). This means that the misrepresentation of the precipitation type is not the major reason for the underestimation bias for the convective cases in the tropics.

For GPROF algorithm, there are only slight reductions of the overestimation bias for the mean condensed water content of the stratiform precipitation (from +42% to +40% in the middle-to-high latitudes and from +63% to +61% in the tropics; Figs. 13b, 13f, 13d, and 13h). It suggests that even if the

#### Mean condensed water content (Conditional on CMB's precip type) a) Mid-high (Conv) C) d) Tropics (Strat) Mid-high (Strat) Tropics (Conv) 0.50 +**q**3% 0.2 0.2 0.2 [g/m3] -14% 0.25 -37% -23% 0.00 0.0 0.0 0.0 EPC EPC GPROF CMB **GPROF** CMB CMB EPC **GPROF** CMB EPC GPROF Mean condensed water content (Correctly classified cases) e) Mid-high (Conv) Mid-high (Strat) Tropics (Conv) Tropics (Strat) 0.50 0.2 0.2 0.2 -18% [g/m3] 0.25



**EPC** 



0.0

CMB

EPC GPROF

FIG. 13. Mean condensed water content and number fraction of correctly classified precipitation type cases. (a)–(d) Mean condensed water content conditioned on the precipitation types by the CMB product. (e)–(h) Mean condensed water content for the cases where both CMB and passive MW products agree in precipitation type. Two bars are shown for the CMB in the middle row. The left bars are the CMB product's mean condensed water content for the cases where CMB and EPC agree in the precipitation type, while the right bars are for the cases of CMB and GPROF pairs. The percentages shown for passive MW products on top and middle rows are the difference from CMB product. Note that the upper limit of the vertical axes of (a) and (e) are different from other panels. (i)–(l) Number fraction of correctly classified cases by each of the passive MW products. In all panels, "Mid-high" refers to the middle to high latitudes (35°–60°N and S) and "Tropics" to 15°S–15°N. The bottom and the top ends of the error bars show the 25th and 75th percentiles. "Conv" and "Strat" refer to convective and stratiform precipitation type, respectively.

precipitation type is correctly represented by the GPROF retrieval, the overestimation bias of the profile magnitude remains. Another point that should be noted is that GPROF in the tropics shows a larger profile magnitude for stratiform precipitation than convective precipitation (Figs. 13g,h), which is contrary to the reference (CMB) data.

0.0

EPC GPROF

0.00

CMB

In summary, a substantial part of the EPC's underestimation of the profile magnitude for the middle-to-high-latitude convective cases is explained by the representation bias of the precipitation type. On the other hand, the other biases of the profile magnitude (i.e., EPC's underestimation for the tropical convective profile magnitude and GPROF's overestimation for the stratiform profile magnitude) would remain even if the precipitation type were correctly represented in the passive MW algorithms. Considering that more than 80% of the precipitation events in the middle-to-high latitudes are stratiform (Fig. 14), the biases for the profile magnitude in the middle-to-high latitudes by the two passive MW algorithms (Fig. 9) are mostly due to the bias in the stratiform precipitation. It should be noted that, however, the convective cases play a significant role for severe weather events even in the middle-to-high

latitudes, and therefore an improved depiction of the convective precipitation is still important. In the tropics, although about a half of the precipitation events are convective (Fig. 14), the GPROF's overestimation of the profile magnitude found in Fig. 9 is mostly due to the significant overestimation for the profile magnitude of stratiform precipitation.

0.0

CMB

EPC GPROF

#### 10. Summary and concluding remarks

This study focused upon the condensed water content profiles estimated by two passive MW-based retrieval algorithms (EPC and GPROF), validated with the GPM radar–radiometer combined (CMB) product as a reference. On average, these passive MW algorithms have biases in the magnitude of the condensed water content profile, notably near the freezing level. The EPC tends to underestimate the profile magnitude especially for the convective type precipitation, whereas GPROF shows systematic overestimation of the magnitude for stratiform cases. The average error of the profile magnitude was found to be smaller for EPC (tropics: less than 20%, middle-to-high latitudes: 20%–50%) than GPROF (tropics: 20%–50% and larger,

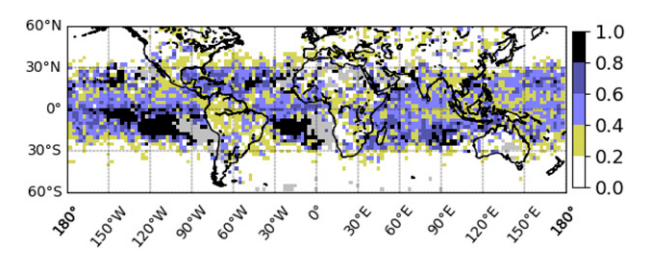


FIG. 14. Number fraction of convective precipitation events estimated by CMB product. The convective precipitation event is defined based on the convective volume fraction.

middle-to-high latitudes: 20%-50%). Some biases of the storm top height were also found. The storm top height defined from the condensed water content profile is slightly underestimated by the EPC and overestimated by the GPROF algorithm. Such biases in the storm top height can be related to the bias in the profile magnitude. Among the biases in the profile magnitude, a substantial portion of the EPC's underestimation for the convective cases in the middle-to-high latitudes can be attributed to the error in the representation of the precipitation type in the algorithms. It has been pointed out by previous studies that the representation error of precipitation type is one of the causes of the passive MW algorithm's estimation error for surface precipitation rate (Petković et al. 2019; Kirstetter et al. 2020). The result of this study suggests that the estimation performance of the vertical precipitation profiles is also affected by the representation error in precipitation type. Such error may be mitigated by the separation technique of the convective and stratiform precipitation developed for the passive MW algorithms (e.g., Petković et al. 2019). It should be noted that the precipitation type information provided by the CMB product, which is used as a reference in this study, may have an error itself (Kirstetter et al. 2020). The analyses using other sources of information, such as ground-based observations, are left for the future study.

Although the profile magnitude is biased, the shapes of the average profile are well reconstructed by the EPC and GPROF algorithms. The agreement between the profile shapes of the CMB product and the passive MW algorithms are particularly good in the middle-to-high-latitude ocean regions, where the average correlation coefficient between the profiles is higher than 0.8 by the EPC and 0.7 by GPROF. The relatively low agreement over land surfaces indicates the relative difficulty in estimating vertical precipitation profiles based solely on passive MW information. However, as for the average profiles, the profile shapes are well captured by the passive MW algorithms even over land regions, with the bias in the height of the peak condensed water content less than 1 km.

The error in the surface precipitation is found to be related to the error in the corresponding profiles. The error in the mean condensed water content shows a clear positive relationship with the surface precipitation error. The correlation coefficients of the profile shapes also show connection with the surface precipitation error. This indicates that physically reasonable connections between surface precipitation and its associated profiles are achieved to some extent in these two

passive MW algorithms. This result also implies that properly constraining physical parameters of the precipitation profiles (e.g., storm top height, freezing level, total condensed water content) would lead to the improvements of the surface precipitation estimates.

One of the motivations in this study to investigate the precipitation profiles by the passive MW algorithms originates from the authors' previous study (Utsumi et al. 2019), which demonstrated that the estimation of the subhourly accumulation of the surface precipitation is improved by taking into account the associated vertical precipitation profile. The realistic representation of the profile shapes by the passive MW algorithms found in this study is encouraging for the application of the abovementioned method to the passive MW-based surface precipitation accumulation, which will contribute to the improvements in the global precipitation monitoring products (e.g., Huffman et al. 2018; Joyce and Xie, 2011; Kubota et al. 2020). Additionally, it will potentially lead to a better understanding of the three-dimensional structure of the precipitating weather systems (Utsumi et al. 2014, 2017) and their evolutions with climate changes (Utsumi et al. 2016).

We focused the analysis only for the observations by GMI in this study. The EPC has been adapted to work with other sensors, including ATMS and MHS cross-track scanning sensors in the GPM constellation, using additional information to account for scan angle dependencies and spatial resolution. Further investigation of the passive MW-based precipitation profile analysis for all passive MW sensors in the GPM constellation is currently underway.

Acknowledgments. The work contained in this manuscript was carried out at the Jet Propulsion Laboratory, California Institute of Technology, under a contract with NASA. Supports from NASA (80NM0018F0617, 80NSSC19K0681, and NNX16AL23G) are recognized. This work is also supported by JAXA's Second Research Announcement on the Earth Observations, JSPS KAKENHI (19K15097 and 18KK0117) and KUAS Research Expenditure for FY 2020 Interdisciplinary Research Activity Support. The support by NSF (Grant EAR-1928724) and NASA (Grant 80NSSC19K0726) to organize the 12th International Precipitation Conference (IPC12), Irvine, California, June 2019, and to produce the IPC12 special collection of papers is also gratefully acknowledged.

Data availability statement. CMB and GPROF dataset are available from NASA's Precipitation Processing System at <a href="https://storm.pps.eosdis.nasa.gov/storm/">https://storm.pps.eosdis.nasa.gov/storm/</a>. EPC and GV-MRMS dataset are too large to be publicly archived with available resources. EPC data are available from Nobuyuki Utsumi (utsumi.nobuyuki@kuas.ac.jp) and GV-MRMS data are available from Pierre-Emmanuel Kirstetter (pierre.kirstetter@noaa.gov).

#### REFERENCES

Aires, F., C. Prigent, F. Bernardo, C. Jiménez, R. Saunders, and P. Brunel, 2011: A Tool to Estimate Land-Surface Emissivities at Microwave frequencies (TELSEM) for use in numerical weather prediction. *Quart. J. Roy. Meteor. Soc.*, 137, 690–699, https://doi.org/10.1002/qj.803.

- Aonashi, K., and R. R. Ferraro, 2020: Microwave sensors, imagers and sounders. *Satellite Precipitation Measurement*, V. Levizzani et al., Eds., Advances in Global Change Research, Vol. 1, Springer, 63–81.
- Awaka, J., M. Le, V. Chandrasekar, N. Yoshida, T. Higashiuwatoko, T. Kubota, and T. Iguchi, 2016: Rain type classification algorithm module for GPM dual-frequency precipitation radar. *J. Atmos. Oceanic Technol.*, 33, 1887–1898, https://doi.org/ 10.1175/JTECH-D-16-0016.1.
- Bauer, P., and A. Mugnai, 2003: Precipitation profile retrievals using temperature-sounding microwave observations. *J. Geophys. Res.*, **108**, 4730, https://doi.org/10.1029/2003JD003572.
- Evans, K. F., J. Turk, T. Wong, and G. L. Stephens, 1995: A Bayesian approach to microwave precipitation profile retrieval. *J. Appl. Meteor.*, **34**, 260–279, https://doi.org/10.1175/1520-0450-34.1.260.
- Gelaro, R., and Coauthors, 2017: The Modern-Era Retrospective Analysis for Research and Applications, version 2 (MERRA-2). J. Climate, 30, 5419–5454, https://doi.org/10.1175/JCLI-D-16-0758.1.
- Grecu, M., W. S. Olson, S. J. Munchak, S. Ringerud, L. Liao, Z. Haddad, B. L. Kelley, and S. F. McLaughlin, 2016: The GPM combined algorithm. J. Atmos. Oceanic Technol., 33, 2225–2245, https://doi.org/10.1175/JTECH-D-16-0019.1.
- Haddad, Z. S., and K.-W. Park, 2009: Vertical profiling of precipitation using passive microwave observations: The main impediment and a proposed solution. *J. Geophys. Res.*, 114, D06118, https://doi.org/10.1029/2008JD010744.
- ——, R. C. Sawaya, S. Kacimi, O. O. Sy, F. J. Turk, and J. Steward, 2017: Interpreting millimeter-wave radiances over tropical convective clouds. *J. Geophys. Res. Atmos.*, **122**, 1650–1664, https://doi.org/10.1002/2016JD025923.
- Heidinger, A. K., C. O'Dell, R. Bennartz, and T. Greenwald, 2006: The successive-order-of-interaction radiative transfer model. Part I: Model development. J. Appl. Meteor. Climatol., 45, 1388–1402, https://doi.org/10.1175/JAM2387.1.
- Hirose, M., and K. Nakamura, 2004: Spatiotemporal variation of the vertical gradient of rainfall rate observed by the TRMM Precipitation Radar. *J. Climate*, **17**, 3378–3397, https://doi.org/10.1175/1520-0442(2004)017<3378:SVOTVG>2.0.CO;2.
- Huffman, G. J., and Coauthors, 2018: NASA Global Precipitation Measurement (GPM) Integrated Multi-satellitE Retrievals for GPM (IMERG). Algorithm Theoretical Basis Doc., version 5.2, 35 pp., https://pmm.nasa.gov/sites/default/files/ document\_files/IMERG\_ATBD\_V5.2\_0.pdf.
- Joyce, R. J., and P. Xie, 2011: Kalman filter-based CMORPH. J. Hydrometeor., 12, 1547–1563, https://doi.org/10.1175/JHM-D-11-022.1.
- Kirstetter, P.-E., and Coauthors, 2012: Toward a framework for systematic error modeling of spaceborne precipitation radar with NOAA/NSSL ground radar-based national mosaic QPE. J. Hydrometeor., 13, 1285–1300, https://doi.org/ 10.1175/JHM-D-11-0139.1.
- ——, W. A. Petersen, and J. J. Gourley, 2018: GPM ground validation Multi-Radar/Multi-Sensor (MRMS) precipitation reanalysis for satellite validation product. NASA Global Hydrology Center DAAC, accessed 19 June 2020, http://doi.org/10.5067/GPMGV/MRMS/DATA101.
- —, —, C. D. Kummerow, and D. B. Wolff, 2020: Integrated multi-satellite evaluation for the global precipitation measurement: Impact of precipitation types on spaceborne precipitation estimation. *Satellite Precipitation Measurement*, V. Levizzani et al., Eds., Advances in Global Change Research, Vol. 2, Springer, 583–608.

- Kobayashi, K., S. Shige, and M. K. Yamamoto, 2018: Vertical gradient of stratiform radar reflectivity below the bright band from the tropics to the extratropical latitudes seen by GPM. *Quart. J. Roy. Meteor. Soc.*, **144**, 165–175, https://doi.org/ 10.1002/qj.3271.
- Kubota, T., and Coauthors, 2020: Global Satellite Mapping of Precipitation (GSMaP) products in the GPM era. *Satellite Precipitation Measurement*, V. Levizzani et al., Eds., Advances in Global Change Research, Vol. 1, Springer, 355–373.
- Kummerow, C. D., D. L. Randel, M. Kulie, N.-Y. Wang, R. Ferraro, S. Joseph Munchak, and V. Petkovic, 2015: The evolution of the Goddard profiling algorithm to a fully parametric scheme. *J. Atmos. Oceanic Technol.*, 32, 2265–2280, https://doi.org/ 10.1175/JTECH-D-15-0039.1.
- Liu, C., and E. J. Zipser, 2013: Why does radar reflectivity tend to increase downward toward the ocean surface, but decrease downward toward the land surface? *J. Geophys. Res. Atmos.*, 118, 135–148, https://doi.org/10.1029/2012JD018134.
- Liu, G., and E.-K. Seo, 2013: Detecting snowfall over land by satellite high-frequency microwave observations: The lack of scattering signature and a statistical approach. *J. Geophys. Res. Atmos.*, **118**, 1376–1387, https://doi.org/10.1002/jgrd.50172.
- Mathew, N., G. Heygster, C. Melsheimer, and L. Kaleschke, 2008: Surface emissivity of Arctic sea ice at AMSU window frequencies. *IEEE Trans. Geosci. Remote Sens.*, 46, 2298–2306, https://doi.org/10.1109/TGRS.2008.916630.
- Passive Microwave Algorithm Team Facility, 2018: Global Precipitation Measurement (GPM) Mission: GPROF2017 Version 1 and Version 2 (used in GPM V5 processing). Algorithm Theoretical Basis Doc., 65 pp., http://rain.atmos.colostate.edu/ATBD/ATBD\_GPM\_V5B\_April15\_2018.pdf.
- Petković, V., M. Orescanin, P. Kirstetter, C. Kummerow, and R. Ferraro, 2019: Enhancing PMW satellite precipitation estimation: Detecting convective class. J. Atmos. Oceanic Technol., 36, 2349–2363, https://doi.org/10.1175/JTECH-D-19-0008.1.
- Ringerud, S., M. S. Kulie, D. L. Randel, G. M. Skofronick-Jackson, and C. D. Kummerow, 2019: Effects of ice particle representation on passive microwave precipitation retrieval in a Bayesian scheme. *IEEE Trans. Geosci. Remote Sens.*, 57, 3619–3632, https://doi.org/10.1109/TGRS.2018.2886063.
- Seo, E.-K., G. Liu, and K.-Y. Kim, 2007: A note on systematic errors in Bayesian retrieval algorithms. *J. Meteor. Soc. Japan*, **85**, 69–74, https://doi.org/10.2151/jmsj.85.69.
- Skofronick-Jackson, G. M., and J. R. Wang, 2000: The estimation of hydrometeor profiles from wideband microwave observations. *J. Appl. Meteor.*, **39**, 1645–1656, https://doi.org/10.1175/1520-0450-39.10.1645.
- —, and Coauthors, 2017: The Global Precipitation Measurement (GPM) mission for science and society. *Bull. Amer. Meteor. Soc.*, **98**, 1679–1695, https://doi.org/10.1175/BAMS-D-15-00306.1.
- Turk, F. J., Z. S. Haddad, and Y. You, 2016: Estimating nonraining surface parameters to assist GPM constellation radiometer precipitation algorithms. J. Atmos. Oceanic Technol., 33, 1333–1353, https://doi.org/10.1175/JTECH-D-15-0229.1.
- —, —, P.-E. Kirstetter, Y. You, and S. Ringerud, 2018: An observationally based method for stratifying a priori passive microwave observations in a Bayesian-based precipitation retrieval framework. *Quart. J. Roy. Meteor. Soc.*, 144, 145–164, https://doi.org/10.1002/qj.3203.
- Utsumi, N., and H. Kim, 2018: Warm season satellite precipitation biases for different cloud types over western North Pacific.

- *IEEE Geosci. Remote Sens. Lett.*, **15**, 808–812, https://doi.org/10.1109/LGRS.2018.2815590.
- —, —, S. Seto, S. Kanae, and T. Oki, 2014: Climatological characteristics of fronts in the western North Pacific based on surface weather charts. *J. Geophys. Res. Atmos.*, **119**, 9400–9418, https://doi.org/10.1002/2014JD021734.
- —, —, S. Kanae, and T. Oki, 2016: Which weather systems are projected to cause future changes in mean and extreme precipitation in CMIP5 simulations? *J. Geophys. Res. Atmos.*, 121, 10 522–10 537, https://doi.org/10.1002/2016JD024939.
- —, —, and —, 2017: Relative contributions of weather systems to mean and extreme global precipitation. J. Geophys. Res. Atmos., 122, 152–167, https://doi.org/ 10.1002/2016JD025222.
- —, —, F. J. Turk, and Z. S. Haddad, 2019: Improving satellite-based subhourly surface rain estimates using vertical rain profile information. *J. Hydrometeor.*, **20**, 1015–1026, https://doi.org/10.1175/JHM-D-18-0225.1.
- Yamamoto, M. K., A. Higuchi, and K. Nakamura, 2006: Vertical and horizontal structure of winter precipitation systems over the western Pacific around Japan using TRMM data. J. Geophys. Res., 111, D13108, https://doi.org/ 10.1029/2005JD006412.
- You, Y., V. Petkovic, J. Tan, R. Kroodsma, W. Berg, C. Kidd, and C. Peters-Lidard, 2020: Evaluation of V05 precipitation estimates from GPM constellation radiometers using KuPR as the reference. *J. Hydrometeor.*, **21**, 705–728, https://doi.org/10.1175/JHM-D-19-0144.1.